# Effect of vertical strain and in-plane biaxial strain on type-II MoSi$_2$N$_4$/Cs$_3$Bi$_2$I$_9$ van der Waals heterostructure

Congying Liu, Zhenwei Wang, Wenqi Xiong, Hongxia Zhong,[a] and Shengjun Yuan[a]

## AFFILIATIONS

Key Laboratory of Artificial Micro- and Nano-structures of Ministry of Education and School of Physics and Technology, Wuhan University, Wuhan 430072, China

[a]Authors to whom correspondence should be addressed: hxzhong@whu.edu.cn and s.yuan@whu.edu.cn

## ABSTRACT

Construction of van der Waals heterostructures (vdWHs) from layered materials may form new types of optoelectronic devices with better performance compared to individual layers. Here, we investigate theoretically the structural stability, electronic properties, charge-transport mechanisms, and optical properties of two-dimensional (2D) MoSi$_2$N$_4$/Cs$_3$Bi$_2$I$_9$ vdWHs by using the first-principles calculations. Our results demonstrate that the 2D MoSi$_2$N$_4$/Cs$_3$Bi$_2$I$_9$ vdWHs possess a direct bandgap and type-II band alignment due to the built-in electric field induced by the electron transfer from MoSi$_2$N$_4$ to Cs$_3$Bi$_2$I$_9$ layer, which can prevent photoinduced electrons and holes from recombination and thus enhance the carrier lifetime. Furthermore, the optical absorption of the heterostructure is enhanced in the visible and ultraviolet region, and its electronic property is tunable under in-plane strains with a clear metal–semiconductor transition. Finally, we explore more A$_3$B$_2$X$_9$/MA$_2$Z$_4$ vdWHs with A = Cs; B = In, Sb, Bi; and X = Cl, Br, I in A$_3$B$_2$X$_9$ and M = Cr, Mo, Ti; A = Si; and Z = N, P in MA$_2$Z$_4$, and we find all three types of band alignments (type-I, type-II, and type-III). Our study provides a comprehensive theoretical understanding of the electronic and optical properties of perovskite-based heterostructures and indicates its potential applications in optoelectronic devices.

## I. INTRODUCTION

In recent years, organic–inorganic lead-based halide perovskites (MAPbX$_3$, X = Cl, Br, I) arose due to their extraordinary electronic properties, especially the excellent light-harvesting capacity,[1–4] and outstanding performance in photovoltaic facilities,[5–10] such as tunable bandgap,[11,12] long carrier diffusion lengths,[13,14] and low synthesis cost.[15–19] A variety of ascendant properties make MAPbX$_3$ the most serviceable materials for fabricating perovskite solar cells.[20] However, MAPbX$_3$ are still far beyond the commercial applications due to their toxicity and instability.[4,21,22] By comparison, the inorganic halide perovskite such as CsPbX$_3$ exhibit much better stability.[23–27] Therefore, the dominating challenge may be resolved by substituting or reducing the amount of lead in perovskite with a disparate and less toxic element. However, many investigations indicate that replacing Pb with nontoxic elements, such as Ge and Sn, may degrade the superior photovoltaic properties and stabilities of

Pb-based halide perovskites. On the other hand, the two-dimensional (2D) trivalent metal-based ternary halide perovskite A$_3$B$_2$X$_9$ (A = MA, Cs; B = Bi, Sb; X = Cl, Br, I)[28–30] is regarded as a new promising material for high performance photovoltaic applications.[31–34] In addition, Bi-based perovskites exhibit better stability and more extensive photovoltaic applications.[35,36] The Bi-based ternary perovskites have larger lattice sizes caused by the presence of two metal ions, which is beneficial to enhance the tenability feature of these materials for the easy ion replacement possibilities. The A$_3$B$_2$X$_9$ compounds have two typical structures: the 0D dimer form composed of isolated [B$_2$X$_9$]$^{3-}$ octahedra and the 2D layered perovskite. The preferential formation of two competing structures depends on the selection of A, B, and X ions.[37,38] Considering that the 0D structure is difficult to form a monolayer and has poor photovoltaic performance,[39] we chose the 2D layered perovskite to construct our heterostructure. The 2D ultrathin few-layer (2–4 layers) nanoplates of Cs$_3$Bi$_2$I$_9$ have been synthesized in

experiments and show high photostability.[40] Previous investigations reported that solar cells fabricated using the $Cs_3Bi_2I_9$ perovskite material showed maximum power conversion efficiency (PCE) is 0.17% for $Cs_3Bi_2I_9$, with an open-circuit voltage of 0.37 eV, short-circuit current density of 1.43 mA/cm$^2$, and fill factor of 32%.[41–45] However, the inferior photovoltaic peculiarities of $Cs_3Bi_2I_9$ perovskite result in its poor manifestation in perovskite solar cell applications,[32] for example, high bandgap, low dielectric constant, and high effective mass.

Much effort has been made to improve the properties of $Cs_3Bi_2I_9$ perovskite solar cells.[46,47] In recent studies, constructing vertical vdWHs[48,49] is found to be an effective method to improve the properties and extend the application range of optoelectronic materials.[50,51] Because of the weak vdW forces, the vdWHs usually preserve the property of each individual component and may form new structures with better physical and chemical properties for device applications.[52–55]

On the other hand, with the rapid advances of experimental techniques, a lot of stable 2D materials with different electronic and optical properties have been realized, such as monolayer $MoSi_2N_4$, which is successfully synthesized very recently using the chemical vapor deposition (CVD) method.[56] $MoSi_2N_4$ is an indirect bandgap semiconductor, which has extraordinary ambient air stability, high electronic and hole mobility, and high strength.[57]

In this manuscript, we construct for the first time, a vdWH consisting of $Cs_3Bi_2I_9$ and $MoSi_2N_4$ monolayers and study its properties with first-principles calculations using the density functional theory. Based on the most stable configuration, we study its electronic structures and charge-transport mechanisms of $MoSi_2N_4/Cs_3Bi_2I_9$ vdWH to investigate its photovoltaic performance. Particularly, we check the regulation of the band structure via applying vertical and in-plane biaxial strain. Then, we calculate the spectrum of optical absorption, which is found to be enhanced drastically in the heterostructure. Finally, we explore more heterostructures of $A_3B_2X_9/MA_2Z_4$ with A = Cs, B = In, Sb, Bi and X = Cl, Br, I in $A_3B_2X_9$ and M = Cr, Mo, Ti, A = Si, and Z = N, P in $MA_2Z_4$ and will show that the band alignment (type-I, type-II, and type-III) can be changed from one to another by adjusting the components in the heterostructures. Our study provides a comprehensive theoretical understanding of the electronic and optical properties of perovskite-based heterostructures and indicates its potential applications in optoelectronic devices besides the pristine perovskite.

## II. CALCULATION METHODS

All structural optimizations and energy calculations are performed by density functional theory (DFT) in a Vienna *ab initio*

simulation package (VASP)[58,59] with the projector augmented-wave (PAW) method.[60] For the exchange-correlation function, the generalized gradient approximation (GGA) within the Perdew–Burke–Ernzerhof (PBE) is applied for structural relaxation.[61] Due to the interference of spin-orbital-coupling (SOC) to heavy atoms, we consider it when calculating the band structure and charge transfer. A kinetic energy cutoff of 520 eV is selected for the plane wave basis set for all calculations, and a $3 \times 3 \times 1$ Monkhorst–Pack $k$ point mesh for the first Brillouin zone integration are utilized to fully optimize geometric structure. The energy convergence threshold is $1.0 \times 10^{-4}$ eV and the criteria for the convergence of the Hellmann–Feynman forces on each atom is 0.05 eV/Å. The vdW interaction, as the main component of long-range contribution, has been investigated widely. We use the popular DFT-D3 functional to describe the vdW interaction. To avoid the interactions between the adjacent slabs, a vacuum region along the z axis is set to 20 Å in our calculations.

## III. RESULTS AND DISCUSSION

To verify the reliability of our results, we first analyze the geometries and electronic structures of monolayer $MoSi_2N_4$ and $Cs_3Bi_2I_9$. The optimized lattice constant of hexagonal $MoSi_2N_4$ ($Cs_3Bi_2I_9$) is 2.90 (8.65) Å in Table I, which agrees well with the value of 2.91 (8.4) Å in previous reports.[57,62] In order to minimize the lattice mismatch of the heterostructure, we adopt a supercell, consisting of $1 \times 1$ $Cs_3Bi_2I_9$ unit cell and $3 \times 3$ $MoSi_2N_4$ primitive cells to construct the $MoSi_2N_4/Cs_3Bi_2I_9$ heterojunction as shown in Figs. 1(a) and 1(b). The lattice mismatch in this vdWH is only 0.227%, which is too small to affect the atomic and electronic structure of the constructed $MoSi_2N_4/Cs_3Bi_2I_9$ heterojunction. Therefore, the results of the designed $MoSi_2N_4/Cs_3Bi_2I_9$ heterojunction are reliable.

In order to find the most stable configuration rather than a local stable system, in Fig. 1(c), we study the evolution of the binding energy ($E_b$) as a function of the interlayer distance ($d$) between $MoSi_2N_4$ and $Cs_3Bi_2I_9$. The binding energy ($E_b$) is calculated by the equation $E_b = (E_{Heter} - E_{MoSi_2N_4} - E_{Cs_3Bi_2I_9})/n$, where $E_{Heter}$, $E_{MoSi_2N_4}$, and $E_{Cs_3Bi_2I_9}$ represent the total energies of $MoSi_2N_4/Cs_3Bi_2I_9$ heterostructure, monolayer $MoSi_2N_4$, and monolayer $Cs_3Bi_2I_9$, respectively, and $n$ is the number of $MoSi_2N_4$ primitive cells.[63] First, for various interlayer distance, the $E_b$ values are negative, indicating that the vdWH can be synthesized in the experiment. Furthermore, when the interlayer distance reaches 3.55 Å, the $E_b$ values is lowest. This equilibrium interlayer distance of vdWHs is similar with 3.60 Å in the $CsPbBr_3/MoS_2$ heterostructure[53] and 3.35 Å (Pb-I terminated) in the $Cs_2PbI_4$/black-phosphorus heterostructure.[54] The equilibrium $d$ suggests a weak vdW interaction

**TABLE I.** The geometric parameters, total energy ($E_{total}$), binding energy ($E_b$), bandgap ($E_g$), work function ($W_F$) and effective mass of $Cs_3Bi_2I_9$ and $MoSi_2N_4$ monolayers and the heterostructure.

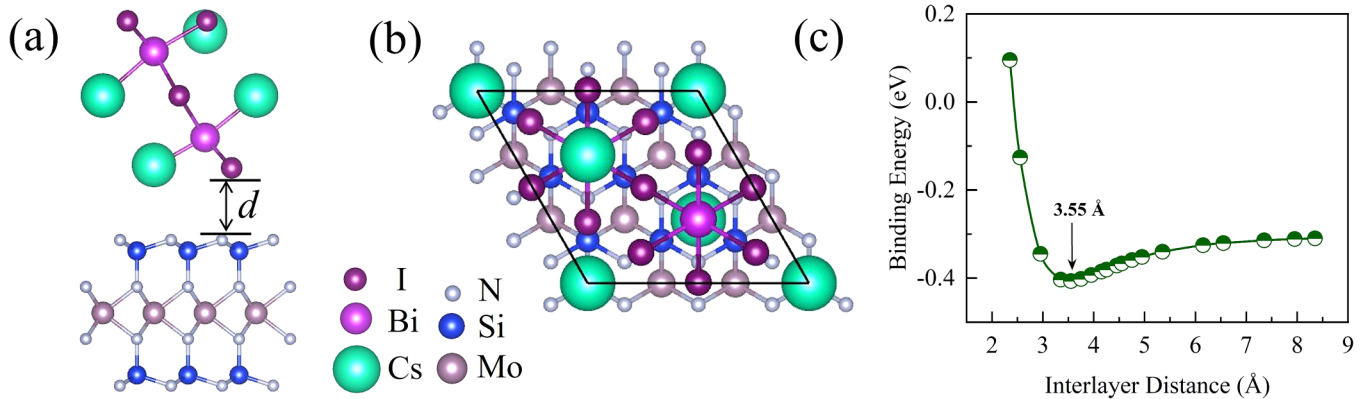| | a (Å) | b (Å) | $E_{total}$ (eV) | $E_b$ (eV) | $E_g$ (eV) | $W_F$ (eV) | $m_e$ | $m_e^\star$ | $m_h$ | $m_h^\star$ |
|---|---|---|---|---|---|---|---|---|---|---|
| $Cs_3Bi_2I_9$ | 8.65 | 8.65 | −40.26 | … | 1.38 | 5.50 | 0.440 | 0.421 | 0.888 | 0.835 |
| $MoSi_2N_4$ | 2.90 | 2.90 | −562.78 | … | 1.79 | 5.11 | 0.451 | 0.625 | 1.128 | 1.168 |
| Heter | 8.66 | 8.66 | −606.70 | −0.41 | 0.91 | 4.88 | 0.298 | 0.300 | 1.538 | 1.547 |

**FIG. 1.** Atomic structure of side view (a) and top view (b) of the $MoSi_2N_4/Cs_3Bi_2I_9$ heterojunction. The Cs, Bi, I, Mo, Si, and N atoms are shown as green, purple, brown, pink, blue, and argent balls, respectively. (c) The variation of binding energy with the interlayer distance of the $MoSi_2N_4/Cs_3Bi_2I_9$ heterostructure.

between the $MoSi_2N_4$ and $Cs_3Bi_2I_9$ layers, which may manifest the electronic properties of the individual layer in the heterostructure. Compared with the bilayer $MoSi_2N_4$, our heterostructure possess direct bandgap and type-II band alignment.[64]

The electronic band structures of $3 \times 3$ $MoSi_2N_4$ supercell, isolated $Cs_3Bi_2I_9$ primitive cell, and $MoSi_2N_4/Cs_3Bi_2I_9$ heterostructure are shown in Fig. 2. In the adopted $3 \times 3$ $MoSi_2N_4$ supercell in Fig. 2(a), compared with the primitive cell, the CBM (VBM) located at the K ($\Gamma$) point of the primitive cell is folded onto the $\Gamma$ ($\Gamma$) point, because of the BZ folding. This leads to the quasi-direct bandgap in the supercell. However, the BZ folding does not affect the bandgap value of 1.79 eV (see Table I), which is consistent with previous results.[57] In Fig. 2(b), monolayer $Cs_3Bi_2I_9$ has a

direct bandgap (1.38 eV) at the $\Gamma$ point, strong electron dispersion at the CBM, but much weak hole dispersion at VBM.[62] The corresponding large hole effective mass is not an ideal condition for solar cell applications.

When the two monolayers are overlaid vertically, we present the projected band structure of the $MoSi_2N_4/Cs_3Bi_2I_9$ heterostructure to analyze the changes. On one hand, the band structure of the heterojunction can be regarded as a simple overlay of the band structures of the individual components, which results from the weak interlayer vdW interaction. On the other hand, $MoSi_2N_4/Cs_3Bi_2I_9$ heterostructure is a direct-bandgap semiconductor, with a bandgap of 0.91 eV at the $\Gamma$ point. The VBM and CBM are contributed by $MoSi_2N_4$ and $Cs_3Bi_2I_9$, respectively. Therefore, the direct bandgap is not caused by the BZ folding, confirming the robust direct feature of vdWHs. The desired direct-bandgap feature is different from the indirect bandgap of pristine monolayer $MoSi_2N_4$. Furthermore, the separate VBM and CBM in Fig. 2(c) suggest the desired type-II heterostructure. For type-II heterostructures, the electrons and holes can be separated in different materials, thereby decreasing the recombination of electron–hole. Typically, type-II band alignment is formed at the interface, with tunable interlayer coupling and ultrafast charge transfer, which provide an ideal platform for promoting the effective separation of photogenerated carriers and facilitating the quantum efficiency.[65–70]

In order to know the interfacial charge transfer, we calculate the charge density difference of the heterostructure, as shown in Figs. 3(a) and 3(b). The three-dimensional charge density difference along the z direction $\Delta\rho(z)$ is defined as $\Delta\rho(z) = \rho(z)_{Heter} - \rho(z)_{MoSi_2N_4} - \rho(z)_{Cs_3Bi_2I_9}$, where $\rho(z)_{Heter}$, $\rho(z)_{MoSi_2N_4}$, and $\rho(z)_{Cs_3Bi_2I_9}$ are charge densities of heterostructure, isolated $MoSi_2N_4$, and isolated $Cs_3Bi_2I_9$, respectively. We can notice that the charge depletion and accumulation are mainly concentrated near the interface area, and the $MoSi_2N_4$ layer is surrounded by the positive charges; meanwhile, the $Cs_3Bi_2I_9$ layer is surrounded by negative charges. This means that electrons migrate from the $MoSi_2N_4$ layer to the $Cs_3Bi_2I_9$ layer through the interfacial area. The electron flow direction is consistent with the result from



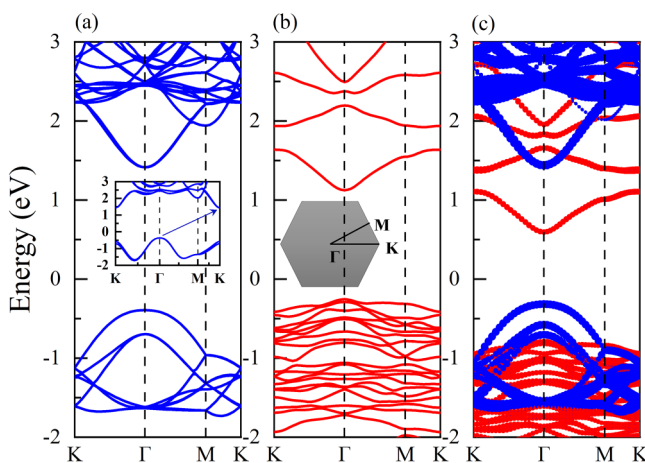**FIG. 2.** Band structures of (a) isolated $MoSi_2N_4$, (b) isolated $Cs_3Bi_2I_9$, and (c) projected band structures of the $MoSi_2N_4/Cs_3Bi_2I_9$ heterostructure. The red and blue lines represent the electronic orbital contributions of $Cs_3Bi_2I_9$ and $MoSi_2N_4$, respectively. The fermi level is set to zero.

the type-II band structure analysis. To further clarify the charge redistribution, we plot the plane-averaged charge density difference $\Delta\rho$ along the vertical direction ($z$ axis) for the heterostructure in Fig. 3(b). Here, $\Delta\rho$ is obtained by the plane-averaged charge density difference between the heterostructure and two noninteracting components. It is observed that there is a negative $\Delta\rho$ near the $MoSi_2N_4$ surface, but a positive $\Delta\rho$ near the $Cs_3Bi_2I_9$ surface. This clearly suggests that the charges deplete at the $MoSi_2N_4$ monolayer and accumulate at $Cs_3Bi_2I_9$ monolayer. Because the charges transfer from $MoSi_2N_4$ to $Cs_3Bi_2I_9$ in the heterojunction, causing the separation of electron–hole pairs, an internal electronic field is generated, which efficiently keeps photoinduced electrons and holes from recombining and extends the lifetime of the carriers in the $MoSi_2N_4/Cs_3Bi_2I_9$ heterostructure.

Energy level shift is a critical parameter to describe the interfacial characteristics, which can further help us to understand the origin of the charge transfer mechanism at the heterostructure interface. We thus plot the energy level of the band edge for the vdWH in Fig. 3(c), using the vacuum level as the energy reference ($E_{vac} = 0$). In the pre-contact state, the values of CBM and VBM in $MoSi_2N_4$ are lower than those in $Cs_3Bi_2I_9$. When they contact with each other, the electrons spontaneously move from $MoSi_2N_4$ to $Cs_3Bi_2I_9$, and the holes flow in the opposite direction. Therefore, the electrons accumulate in the $Cs_3Bi_2I_9$ interface and the holes accumulate in the $MoSi_2N_4$ interface, which leads to the decrease

(increase) in the interface electric potential in the interface. This confirms the charge transfer path in Figs. 3(a) and 3(b) again. The electron flow is driven by the work function, and the work function of isolated $MoSi_2N_4$, isolated $Cs_3Bi_2I_9$, and $MoSi_2N_4/Cs_3Bi_2I_9$ heterostructure are calculated to be 5.11, 5.50, and 4.88 eV, respectively (as shown in Table I). When two semiconductors contact to form a heterojunction, the work function in the different monolayers must be consistent. Because the work function of $Cs_3Bi_2I_9$ is higher than that of $MoSi_2N_4$, the positive-charges attach to $MoSi_2N_4$, while the negative-charges accumulate in $Cs_3Bi_2I_9$, generating a build-in electric field pointing from the $MoSi_2N_4$ layer to the $Cs_3Bi_2I_9$ layer. The electrons and holes drift in the internal electric field as opposed to the diffusion action, ultimately the diffusion and drift of carriers come up to a dynamic balance. In type-II $MoSi_2N_4/Cs_3Bi_2I_9$ heterostructure, the electrons and holes are separated in different layers, and the recombination of electrons and holes is reduced, which is more suitable for photodetectors and solar cells.

Applying vertical strain is an effective approach to modify the electronic properties of layered heterostructures. The vertical stain can be realized by hydrostatic pressure,[71] nanomechanical pressures, or via inserting layered insulators.[72] In our model, the vertical strain is implemented by changing interlayer distance from 2.55 to 8.35 Å. Figure 4(a) exhibits the variation of the bandgap of $MoSi_2N_4/Cs_3Bi_2I_9$ heterostructure as a function of the interlayer distance. When the interlayer distance is larger than the equilibrium distance,



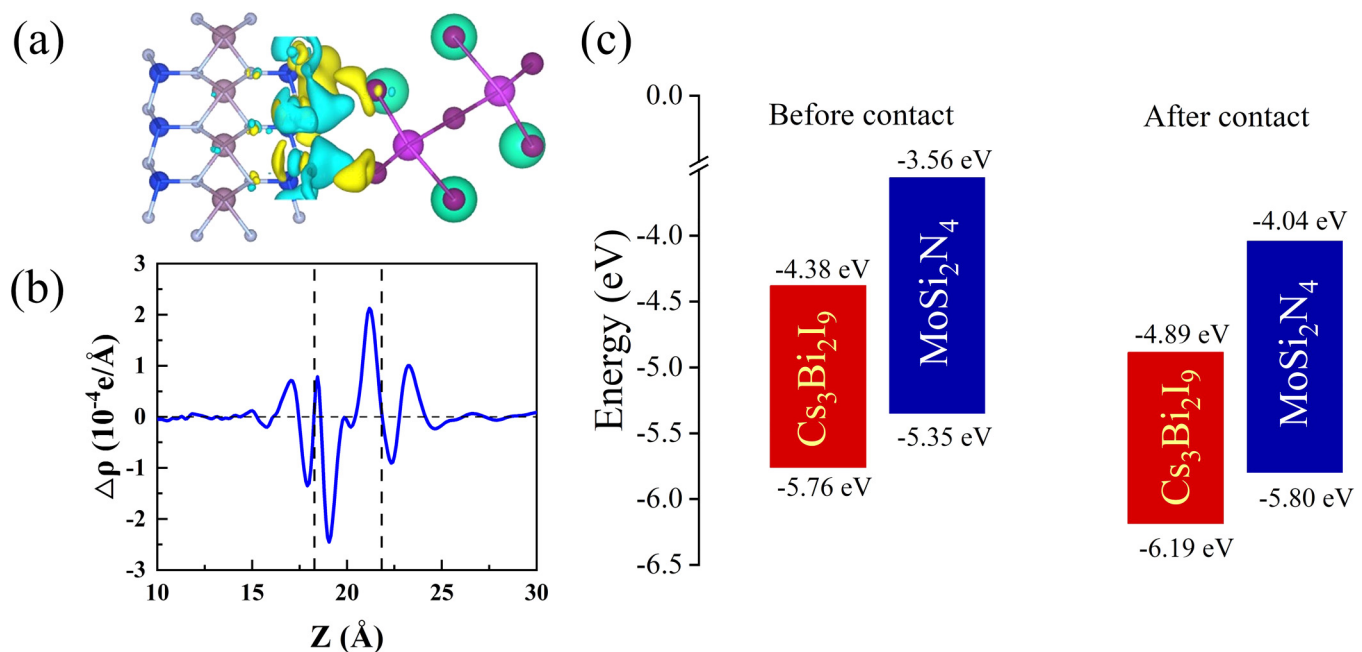FIG. 3. (a) The 3D charge density difference of $MoSi_2N_4/Cs_3Bi_2I_9$. The yellow and cyan regions represent the charge accumulation and depletion in the space, respectively. (b) The planar-averaged charge density difference $\Delta\rho$ of the $MoSi_2N_4/Cs_3Bi_2I_9$ heterojunction. (c) Schematic energy level diagrams of the $MoSi_2N_4/Cs_3Bi_2I_9$ heterostructure in the pre-contact and after-contact states. Here, "Before-contact" and "After-contact" refer to the band energies in the individual layers and heterostructure, respectively, and the vacuum energy is set to zero. The top and bottom of the rectangles represent the values of VBM and CBM. The blue and red rectangles represent the energy levels of $MoSi_2N_4$ and $Cs_3Bi_2I_9$, respectively.

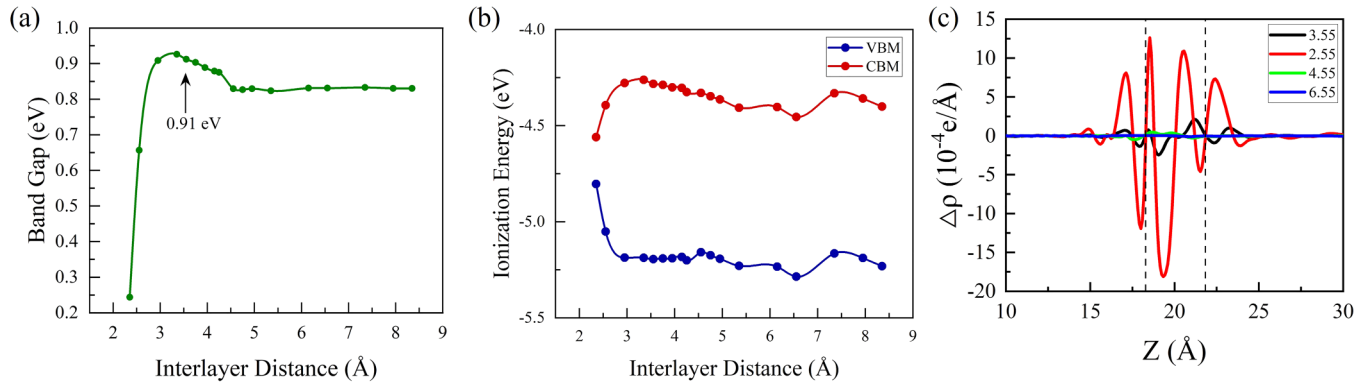**FIG. 4.** (a) Variation of bandgap with the interlayer distance of the $MoSi_2N_4/Cs_3Bi_2I_9$ heterostructure. (b) The band edge alignments of the $MoSi_2N_4/Cs_3Bi_2I_9$ heterostructure with different interlayer distances. The vacuum energy is set to zero. (c) The differential charge density of the $MoSi_2N_4/Cs_3Bi_2I_9$ heterostructure at difference interlayer distances.

the bandgap keeps almost the same, indicating that the interlayer interaction is too weak to affect the electronic properties. While the interlayer distance is smaller than the equilibrium distance, the bandgap first increases sharply and then decreases. The largest direct bandgap is 0.93 eV for the case of $d = 3.35$ Å. Moreover, when $d$ is smaller than 2.55 Å, the direct bandgap turns into an indirect one, and the indirect–direct bandgap transition of the heterostructure may be contributed to the orbital overlap and interlayer coupling. Therefore, the bandgap value and feature can be modified efficiently by applying vertical strain. Figure 4(b) exhibits the band edge alignments of the $MoSi_2N_4/Cs_3Bi_2I_9$ heterostructure with different interlayer distances. With the increase in interlayer distance, both the CBM and VBM are driven continuously toward or off the Fermi level, leading to the diminution or enlargement of bandgap. But for 2.95 Å $< d <$ 3.95 Å, the decrease of bandgap is caused by CBM shifting off Fermi level and VBM shifting toward the Fermi level. Furthermore, when the interlayer distance is more than 4.55 Å, the CBM keeps pace with VBM with the variation of interlayer distance. The calculated band edge energy levels provide guidance for constructing heterojunction and matching with electron transport layer and hole transport layer in solar cell devices.

To comprehensively investigate the effects of vertical strain on the electronic structure in the $MoSi_2N_4/Cs_3Bi_2I_9$ heterostructure, Fig. 4(c) presents the plane-averaged charge density difference $\Delta\rho$ of the heterojunction at different interlayer distances, indicating that the charge redistribution in the interface region sensitively depends on the interlayer distance. The smaller the interlayer distance is, the larger the change transfer is between interfaces. $\Delta\rho$ of the equilibrium distance is nearly zero for the whole $z$ coordinate in comparison with narrowing interlayer distances, indicating that there is almost no charge transfer between $MoSi_2N_4$ and $Cs_3Bi_2I_9$ layers. This is also consistent with the observed very weak interlayer vdW interaction in the $MoSi_2N_4/Cs_3Bi_2I_9$ heterostructure. For narrowed interlayer distances of the $MoSi_2N_4/Cs_3Bi_2I_9$ heterostructure, a charge transfer of $10^{-3}$ e/Å magnitude is observed, which demonstrates that the photo-generated electrons and holes can easily

transfer across the hetero-interface, resulting in a stronger interaction between $MoSi_2N_4$ and $Cs_3Bi_2I_9$ layers.

Besides vertical strain, in-plane mechanical strain is also a powerful tool to modulate the electronic and transport properties of heterostructures, which has been verified in many previous reports.[73,74] Therefore, we investigate the effect of biaxial strain on the $MoSi_2N_4/Cs_3Bi_2I_9$ heterostructure via altering the lattice constant of X axis and Y axis simultaneously. The biaxial strain $\varepsilon$ is defined as $\varepsilon = \left[\frac{a-a_0}{a_0}\right] \times 100\%$, where $a$ and $a_0$ represent the lattice constants of the hetero-bilayer with and without strain, respectively. Therefore, the positive value ($\varepsilon > 0$) signifies tensile strain, and the negative value ($\varepsilon < 0$) represents compressive strain. To make sure that the applied biaxial strains are under the elastic response range, we also calculate the strain energies of per atom as $E_s = \frac{(E_{strained}-E_{unstrained})}{n}$, where $E_{strained}$ and $E_{unstrained}$ represent the total energies with and without biaxial strain, and $n$ is the total atom number of hetero-bilayer.

Figure 5 shows the variation of strain energies of the $MoSi_2N_4/Cs_3Bi_2I_9$ heterostructure with the biaxial strains. For both compressive and tensile strain, the strain energy increases monotonously with the enhancement of biaxial strain. Moreover, the biaxial strain is in a perfect quadratic function with the strain energy, indicating that the geometric structure of the heterostructure is not destroyed under biaxial strain. Thus, the system is flexible. The process is completely reversible and all the strains considered are within the elastic limit.[75] On the other hand, with the enhancement of tensile (compressive) strain strength, the bandgap increases first to a maximum value of 0.997 eV (1.387 eV) at $\varepsilon = 3\%$ ($\varepsilon = -7\%$). If we continuously increase the biaxial strain, the direct bandgap turns into indirect, and an electronic phase transition from a semiconductor to metal is observed when $\varepsilon = -12\%$ with a positive binding energy. The supercell of the heterostructure contains 77 electrons, which is computationally too large for the phonon spectrum calculation. It is possible that the *P-3m1* structure with 10% strain may not be in the ground state, but the stability of the structure can be increased by choosing a
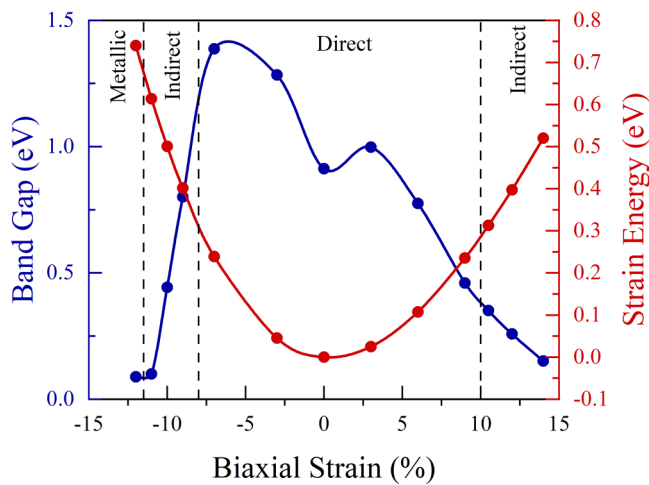
**FIG. 5.** The variation of bandgap and strain energy of the MoSi$_2$N$_4$/Cs$_3$Bi$_2$I$_9$ heterostructure as a function of the biaxial strain.

proper substrate. For example, although bilayer borophene is not stable,[76] it can be fabricated on the Cu (111) surface[77] or Au (111) surface.[78] We postpone the theoretical study of substrate-induced stabilization in future. The diminution of bandgap is owing to the increasing charge amount passing through the interface between MoSi$_2$N$_4$ and Cs$_3$Bi$_2$I$_9$ layers. Obviously, the bandgap of the MoSi$_2$N$_4$/Cs$_3$Bi$_2$I$_9$ heterostructure can be efficiently tuned by applying moderate biaxial strain.

Furthermore, to comprehensively investigate the semiconductor–metal phase transition and the effect of biaxial strain of the heterostructure, we calculate corresponding projected band structures of the MoSi$_2$N$_4$/Cs$_3$Bi$_2$I$_9$ heterostructure at different biaxial strain strengths in Figs. 6(a)–6(f). With the enhancement of compressive strain, the CBM (contributed by MoSi$_2$N$_4$) goes downward, and the VBM (contributed by Cs$_3$Bi$_2$I$_9$) goes upward, leading to the reduction of bandgap. However, for tensile strain, the band alignment changed from type-II to type-I; moreover, the CBM and VBM (both contributed by MoSi$_2$N$_4$) approach the Fermi level simultaneously and finally causing the semiconductor–metal phase transition. In other words, the contribution of band edges can be regulated and controlled by tensile strain, and maintain type-I band alignment at the same time. By the reason of foregoing, applying biaxial strain is a significant strategy for modifying the characteristic of the MoSi$_2$N$_4$/Cs$_3$Bi$_2$I$_9$ heterojunction in practical applications, which plays a momentous part in high performance electronic and optoelectronic apparatus.

In order to analyze the optical properties of MoSi$_2$N$_4$ and Cs$_3$Bi$_2$I$_9$ combination, we calculate the optical absorptions of monolayer MoSi$_2$N$_4$, monolayer Cs$_3$Bi$_2$I$_9$, and MoSi$_2$N$_4$/Cs$_3$Bi$_2$I$_9$ heterostructure in Fig. 7. The absorption coefficient $\alpha(\omega)$ is defined as
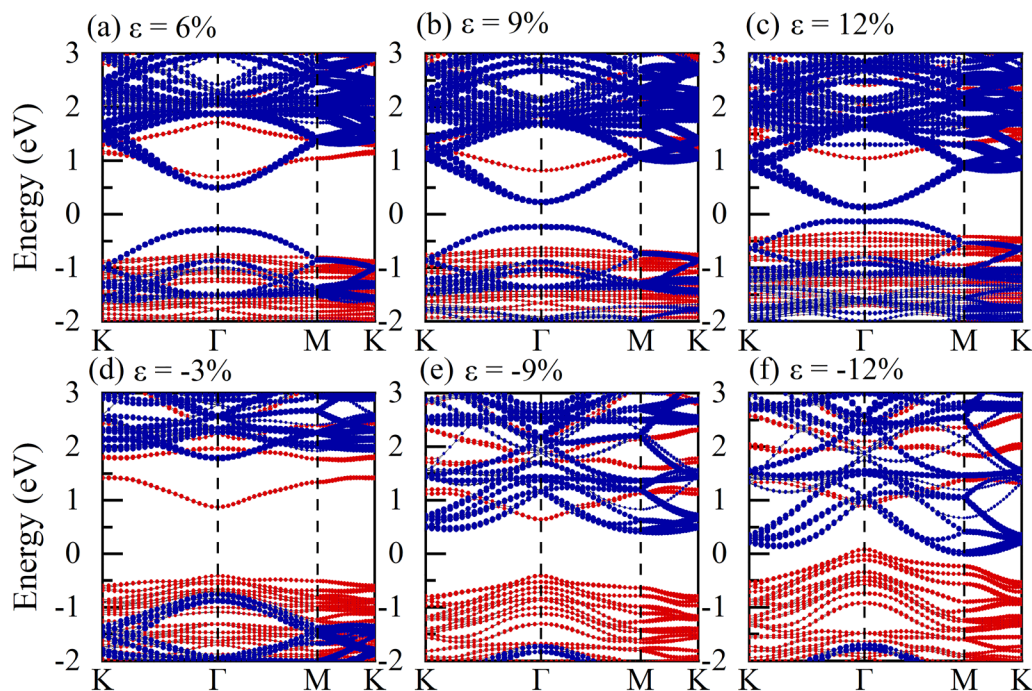


**FIG. 6.** Projected band structures of MoSi$_2$N$_4$/Cs$_3$Bi$_2$I$_9$ heterostructure at representative biaxial strains of (a) 6%, (b) −9%, (c) 12%, (d) −3%, (e) −9%, and (f) −12%, respectively. The red and blue lines represent the electronic orbital contributions of Cs$_3$Bi$_2$I$_9$ and MoSi$_2$N$_4$, respectively. The fermi level is set to zero.

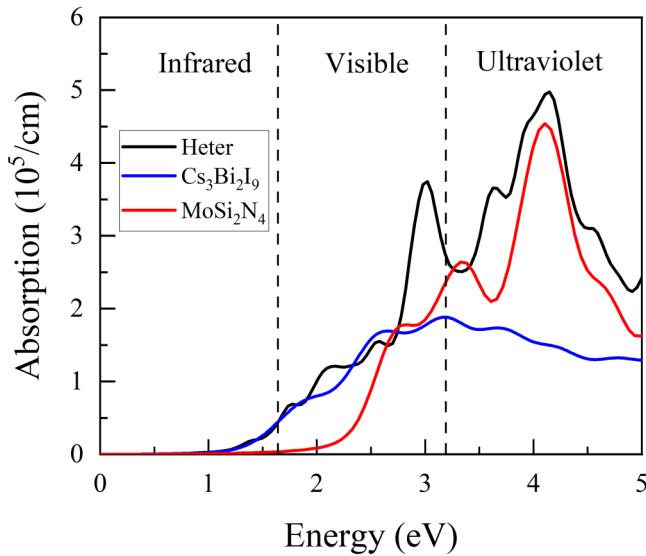**FIG. 7.** Calculated absorption coefficients of monolayer $MoSi_2N_4$, monolayer $Cs_3Bi_2I_9$, and $MoSi_2N_4/Cs_3Bi_2I_9$ heterostructure.

the following formula: $\alpha(\omega) = \sqrt{2}\omega \left[ \sqrt{\varepsilon_1(\omega)^2 + \varepsilon_2(\omega)^2} - \varepsilon_1(\omega) \right]^{\frac{1}{2}}$, where $\varepsilon_1(\omega)$ and $\varepsilon_2(\omega)$ are the real and imaginary parts of the dielectric function, respectively, depending on the optical frequency $\omega$. It can be clearly seen from Fig. 7 that the light abilities of $Cs_3Bi_2I_9$ are effectively enhanced by the vdWH, especially in the ultraviolet region. The $MoSi_2N_4/Cs_3Bi_2I_9$ heterojunction has a wide
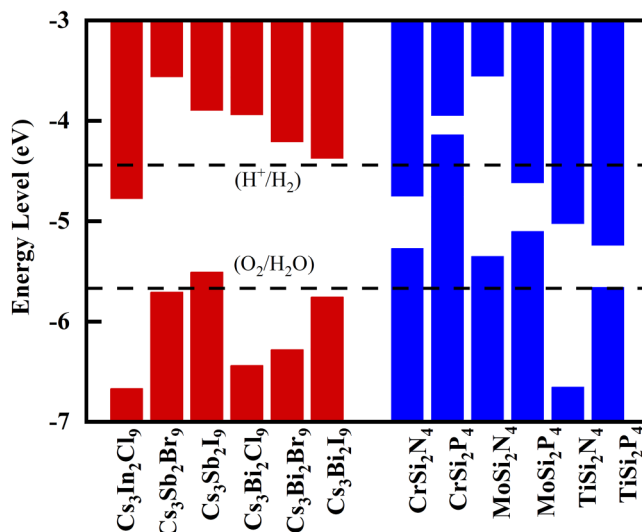


**FIG. 8.** Band diagrams of perovskites-$A_3B_2X_9$ (A = Cs; B = In, Sb, Bi; X = Cl, Br, I) and $MA_2Z_4$ (M = Cr, Mo, Ti; A = Si; Z = N, P). The vacuum level is set to zero.

absorption range and the optical absorption magnitude can reach $10^5$ cm$^{-1}$, which is much higher than that of the $CsPbI_3/MS_2$ heterostructure.[55] The increase of absorption of the $MoSi_2N_4/Cs_3Bi_2I_9$ heterojunction, compared with monolayer $MoSi_2N_4$ and monolayer $Cs_3Bi_2I_9$, is due to the electron transition from $MoSi_2N_4$ to $Cs_3Bi_2I_9$. Hence, it is an efficient way to strengthen optical absorption and obtain excellent photovoltaic properties by building vdWHs. Furthermore, the $MoSi_2N_4/Cs_3Bi_2I_9$ heterojunction can harvest solar energy effectively, due to its outstanding photocatalytic performance in the visible light region.

To get a general conclusion, we summarize the band energy levels of perovskites $A_3B_2X_9$ (A = Cs; B = In, Sb, Bi; X = Cl, Br, I) and $MA_2Z_4$ (M = Cr, Mo, Ti; A = Si; Z = N, P) in Fig. 8. It is shown that type-I, type-II, and type-III $A_3B_2X_9/MA_2Z_4$ can be formed. For example, $CrSi_2N_4$ and $MoSi_2P_4$ tend to form a type-I band alignment for all $A_3B_2X_9$, while type-II band alignment dominates in the vdWHs between $A_3B_2X_9$ and $MoSi_2N_4$ and $TiSi_2N_4$; moreover, $CrSi_2P_4$ can form type-III band alignment. Generally, type-I band alignments are most widely utilized in optical devices, such as light-emitting diodes and in lasers as they provide a means to spatially confine electrons and holes so that efficient recombination can occur, and type-II band alignments are very useful for unipolar electronic device applications since they allow larger offsets on one side, thus allowing extremely strong carrier confinement. Type-II and type-III heterostructures are also useful to engineer the conduction to valence band transition energy. This is particularly important in tunneling field effect transistors in order to enhance the tunneling current density, as well as in infrared intersubband superlattice lasers and wavelength photodetectors. Therefore, vdWHs $A_3B_2X_9/MA_2Z_4$ can satisfy all the requirements for different band alignment types. Furthermore, some $A_3B_2X_9/MA_2Z_4$ vdWHs exhibit VBM lower than the redox potential of $O_2/H_2O$ (−5.67 eV), and CBM higher than the redox potential of $H^+/H_2$ (−4.44 eV), suggesting that the overall water splitting can be achieved in the vdWHs photocatalyst under visible-light irradiation. Finally, we have to point out that the electronic structures of all the constructed $A_3B_2X_9/MA_2Z_4$ vdWHs can be regulated effectively by vertical and in-plane biaxial strains, such as bandgaps and charge densities.

## IV. CONCLUSIONS

In this work, we theoretically investigate the geometric structure, charge transfer, electronic, and optical properties of the $MoSi_2N_4/Cs_3Bi_2I_9$ vdWH based on first-principles calculations. The negative binding energy indicates that the $MoSi_2N_4/Cs_3Bi_2I_9$ heterojunction can be experimentally prepared. Furthermore, the heterostructure is a semiconductor with a direct bandgap of 0.91 eV at the Γ point possessing a type-II band alignment, which can promote spatial effective separation of photo-generated carrier pairs. Accordingly, the electrons transfer from $MoSi_2N_4$ layer to $Cs_3Bi_2I_9$ layer, generating a built-in electric field, preventing photo-induced electrons and holes from recombination, and enhancing the lifetime of the carriers. More significantly, both vertical strain and in-plane biaxial strain can efficiently modulate the electronic properties of the $MoSi_2N_4/Cs_3Bi_2I_9$ heterostructure. In addition, the optical absorption ($10^5$ cm$^{-1}$) of the heterostructure is

enhanced in the visible and ultraviolet region. Finally, by adjusting the components of heterostructures, type-I, type-II, and type-III $A_3B_2X_9/MA_2Z_4$ vdWHs (A = Cs; B = In, Sb, Bi; X = Cl, Br, I; M = Cr, Mo, Ti; A = Si; Z = N, P) can be formed, satisfying all the requirements for different applications. The current work concludes with a $MoSi_2N_4/Cs_3Bi_2I_9$ heterostructure with a stable structure and excellent photoelectric properties, and it provides some guidance for the design of photoelectric devices, heterojunction devices, and infrared light conversion and detection.

## DATA AVAILABILITY

See the supplementary material for the complete study with different stacking patterns and vdW functionals.

## ACKNOWLEDGMENTS

## AUTHOR DECLARATIONS
### Conflict of Interest

The authors declare that they have no known competing financial interest or personal relationships that could have appeared to influence the work reported in this paper.

## DATA AVAILABILITY

The data that support the findings of this study are available from the corresponding authors upon reasonable request.

## REFERENCES

[1]H. J. Snaith, "Perovskites: The emergence of a new era for low-cost, high-efficiency solar cells," J. Phys. Chem. Lett. **4**(21), 3623–3630 (2013).
[2]J. Burschka, N. Pellet, S.-J. Moon, R. Humphry-Baker, P. Gao, M. K. Nazeeruddin, and M. Grätzel, "Sequential deposition as a route to high-performance perovskite-sensitized solar cells," Nature **499**(7458), 316–319 (2013).
[3]I. Mesquita, L. Andrade, and A. Mendes, "Perovskite solar cells: Materials, configurations and stability," Renew. Sustain. Energy Rev. **82**, 2471–2489 (2018).
[4]A. Kojima, K. Teshima, Y. Shirai, and T. Miyasaka, "Organometal halide perovskites as visible-light sensitizers for photovoltaic cells," J. Am. Chem. Soc. **131**(17), 6050–6051 (2009).
[5]L. Protesescu, S. Yakunin, M. I. Bodnarchuk, F. Krieg, R. Caputo, C. H. Hendon, R. X. Yang, A. Walsh, and M. V. Kovalenko, "Nanocrystals of cesium lead halide perovskites ($CsPbX_3$, X = Cl, Br, and I): Novel optoelectronic materials showing bright emission with wide color gamut," Nano Lett. **15**(6), 3692–3696 (2015).
[6]J. Song, J. Li, X. Li, L. Xu, Y. Dong, and H. Zeng, "Quantum dot light-emitting diodes based on inorganic perovskite cesium lead halides ($CsPbX_3$)," Adv. Mater. **27**(44), 7162–7167 (2015).
[7]T. Guner and M. M. Demir, "A review on halide perovskites as color conversion layers in white light emitting diode applications," Phys. Stat. Solidi A **215**(13), 1800120 (2018).
[8]X. Li, F. Cao, D. Yu, J. Chen, Z. Sun, Y. Shen, Y. Zhu, L. Wang, Y. Wei, Y. Wu, and H. Zeng, "All inorganic halide perovskites nanosystem: Synthesis, structural features, optical properties and optoelectronic applications," Small **13**(9), 1603996 (2017).

[9]X. He, Y. Qiu, and S. Yang, "Fully-inorganic trihalide perovskite nanocrystals: A new research frontier of optoelectronic materials," Adv. Mater. **29**(32), 1700775 (2017).
[10]H. Huang, L. Polavarapu, J. A. Sichert, A. S. Susha, A. S. Urban, and A. L. Rogach, "Colloidal lead halide perovskite nanocrystals: Synthesis, optical properties and applications," NPG Asia Mater. **8**(11), e328(2016).
[11]J. H. Noh, S. H. Im, J. H. Heo, T. N. Mandal, and S. I. Seok, "Chemical management for colorful, efficient, and stable inorganic-organic hybrid nanostructured solar cells," Nano Lett. **13**(4), 1764–1769 (2013).
[12]W.-J. Yin, J.-H. Yang, J. Kang, Y. Yan, and S.-H. Wei, "Halide perovskite materials for solar cells: A theoretical review," J. Mater. Chem. A **3**(17), 8926–8942 (2015).
[13]S. D. Stranks, G. E. Eperon, G. Grancini, C. Menelaou, M. J. P. Alcocer, T. Leijtens, L. M. Herz, A. Petrozza, and H. J. Snaith, "Electron-hole diffusion lengths exceeding 1 micrometer in an organometal trihalide perovskite absorber," Science **342**(6156), 341–344 (2013).
[14]Q. Dong, Y. Fang, Y. Shao, P. Mulligan, J. Qiu, L. Cao, and J. Huang, Electron-hole diffusion lengths &gt; 175 $\mu m$ in solution-grown $CH_3NH_3PbI_3$ single crystals. Science 2015, **347** (6225), 967–970.
[15]M. Liu, M. B. Johnston, and H. J. Snaith, "Efficient planar heterojunction perovskite solar cells by vapour deposition," Nature **501**(7467), 395–398 (2013).
[16]O. Malinkiewicz, A. Yella, Y. H. Lee, G. M. Espallargas, M. Graetzel, M. K. Nazeeruddin, and H. J. Bolink, "Perovskite solar cells employing organic charge-transport layers," Nat. Photonics **8**(2), 128–132 (2014).
[17]C.-W. Chen, H.-W. Kang, S.-Y. Hsiao, P.-F. Yang, K.-M. Chiang, and H.-W. Lin, "Efficient and uniform planar-type perovskite solar cells by simple sequential vacuum deposition," Adv. Mater. **26**(38), 6647–6652 (2014).
[18]F. Wang, H. Yu, H. Xu, and N. Zhao, "$HPbI_3$: A new precursor compound for highly efficient solution-processed perovskite solar cells," Adv. Funct. Mater. **25**(7), 1120–1126 (2015).
[19]T. Singh and T. Miyasaka, "High performance perovskite solar cell via multi-cycle low temperature processing of lead acetate precursor solutions," Chem. Commun. **52**(26), 4784–4787 (2016).
[20]S. Govinda, B. P. Kore, M. Bokdam, P. Mahale, A. Kumar, S. Pal, B. Bhattacharyya, J. Lahnsteiner, G. Kresse, C. Franchini, A. Pandey, and D. D. Sarma, "Behavior of methylammonium dipoles in $MAPbX_3$ (X = Br and I)," J. Phys. Chem. Lett. **8**(17), 4113–4121 (2017).
[21]N. K. Noel, S. D. Stranks, A. Abate, C. Wehrenfennig, S. Guarnera, A.-A. Haghighirad, A. Sadhanala, G. E. Eperon, S. K. Pathak, M. B. Johnston, A. Petrozza, L. M. Herz, and H. J. Snaith, "Lead-free organic-inorganic tin halide perovskites for photovoltaic applications," Energy Environ. Sci. **7**(9), 3061–3068 (2014).
[22]K. Qin, B. Dong, and S. Wang, "Improving the stability of metal halide perovskite solar cells from material to structure," J. Energy Chem. **33**, 90–99 (2019).
[23]M. Kulbak, S. Gupta, N. Kedem, I. Levine, T. Bendikov, G. Hodes, and D. Cahen, "Cesium enhances long-term stability of lead bromide perovskite-based solar cells," J. Phys. Chem. Lett. **7**(1), 167–172 (2016).
[24]J. Liang, G. Zhu, C. Wang, P. Zhao, Y. Wang, Y. Hu, L. Ma, Z. Tie, J. Liu, and Z. Jin, "An All-inorganic perovskite solar capacitor for efficient and stable spontaneous photocharging," Nano Energy **52**, 239–245 (2018).
[25]J. Ren, T. Li, X. Zhou, X. Dong, A. V. Shorokhov, M. B. Semenov, V. D. Krevchik, and Y. Wang, "Encapsulating all-inorganic perovskite quantum dots into mesoporous metal organic frameworks with significantly enhanced stability for optoelectronic applications," Chem. Eng. J. **358**, 30–39 (2019).
[26]M. I. Asghar, J. Zhang, H. Wang, and P. D. Lund, "Device stability of perovskite solar cells—A review," Renew. Sustain. Energy Rev. **77**, 131–146 (2017).
[27]P. Banerjee, N. S. Kumar, K. C. B. Naidu, A. Franco, and R. Dachepalli, "Stability of 2D and 3D perovskites due to inhibition of light-induced decomposition," J. Electron. Mater. **49**(12), 7072–7084 (2020).
[28]B. Saparov, F. Hong, J.-P. Sun, H.-S. Duan, W. Meng, S. Cameron, I. G. Hill, Y. Yan, and D. B. Mitzi, "Thin-film preparation and characterization of $Cs_3Sb_2I_9$: A lead-free layered perovskite semiconductor," Chem. Mater. **27**(16), 5622–5632 (2015).

[29]A. J. Lehner, D. H. Fabini, H. A. Evans, C.-A. Hébert, S. R. Smock, J. Hu, H. Wang, J. W. Zwanziger, M. L. Chabinyc, and R. Seshadri, "Crystal and electronic structures of complex bismuth iodides $A_3Bi_2I_9$ (A = K, Rb, Cs) related to perovskite: Aiding the rational design of photovoltaics," Chem. Mater. **27**(20), 7137–7148 (2015).

[30]Z. Ma, S. Peng, Y. Wu, X. Fang, X. Chen, X. Jia, K. Zhang, N. Yuan, J. Ding, and N. Dai, "Air-Stable layered bismuth-based perovskite-like materials: Structures and semiconductor properties," Phys. B Condens. Matter **526**, 136–142 (2017).

[31]B.-W. Park, B. Philippe, X. Zhang, H. Rensmo, G. Boschloo, and E. M. J. Johansson, "Bismuth based hybrid perovskites $A_3Bi_2I_9$(A: Methylammonium or cesium) for solar cell application," Adv. Mater. **27**(43), 6806–6813 (2015).

[32]B. Ghosh, B. Wu, H. K. Mulmudi, C. Guet, K. Weber, T. C. Sum, S. Mhaisalkar, and N. Mathews, "Limitations of $Cs_3Bi_2I_9$ as lead-free photovoltaic absorber materials," ACS Appl. Mater. Interfaces **10**(41), 35000–35007 (2018).

[33]A. Nilă, M. Baibarac, A. Matea, R. Mitran, and I. Baltog, "Exciton-phonon interactions in the $Cs_3Bi_2I_9$ crystal structure revealed by Raman spectroscopic studies," Phys. Status Solidi B **254**(4), 1552805 (2017).

[34]K.-H. Hong, J. Kim, L. Debbichi, H. Kim, and S. H. Im, "Band gap engineering of $Cs_3Bi_2I_9$ perovskites with trivalent atoms using a dual metal cation," J. Phys. Chem. C **121**(1), 969–974 (2017).

[35]L. Liang and P. Gao, "Lead-Free hybrid perovskite absorbers for viable application: Can we eat the cake and have it too?," Adv. Sci. **5**(2), 1700331 (2018).

[36]T. Singh, A. Kulkarni, M. Ikegami, and T. Miyasaka, "Effect of electron transporting layer on bismuth-based lead-free perovskite $(CH_3NH_3)_3Bi_2I_9$ for photovoltaic applications," ACS Appl. Mater. Interfaces **8**(23), 14542–14547 (2016).

[37]K. M. McCall, C. C. Stoumpos, O. Y. Kontsevoi, G. C. B. Alexander, B. W. Wessels, and M. G. Kanatzidis, "From 0D $Cs_3Bi_2I_9$ to 2D $Cs_3Bi_2I_6Cl_3$: Dimensional expansion induces a direct band Gap but enhances electron-phonon coupling," Chem. Mater. **31**(7), 2644–2650 (2019).

[38]C. Tan, X. Cao, X.-J. Wu, Q. He, J. Yang, X. Zhang, J. Chen, W. Zhao, S. Han, G.-H. Nam, M. Sindoro, and H. Zhang, "Recent advances in ultrathin two-dimensional nanomaterials," Chem. Rev. **117**(9), 6225–6331 (2017).

[39]B. Ghosh, S. Chakraborty, H. Wei, C. Guet, S. Li, S. Mhaisalkar, and N. Mathews, "Poor photovoltaic performance of $Cs_3Bi_2I_9$: An insight through first-principles calculations," J. Phys. Chem. C **121**(32), 17062–17067 (2017).

[40]A. Sarkar, P. Acharyya, R. Sasmal, P. Pal, S. S. Agasti, and K. Biswas, "Synthesis of ultrathin few-layer 2D nanoplates of halide perovskite $Cs_3Bi_2I_9$ and single-nanoplate super-resolved fluorescence microscopy," Inorg. Chem. **57**(24), 15558–15565 (2018).

[41]R. Waykar, A. Bhorde, S. Nair, S. Pandharkar, B. Gabhale, R. Aher, S. Rondiya, A. Waghmare, V. Doiphode, A. Punde, P. Vairale, M. Prasad, and S. Jadkar, "Environmentally stable lead-free cesium bismuth iodide $(Cs_3Bi_2I_9)$ perovskite: Synthesis to solar cell application," J. Phys. Chem. Solids **146**, 109608 (2020).

[42]M. T. Islam, M. R. Jani, K. M. Shorowordi, Z. Hoque, A. M. Gokcek, V. Vattipally, S. S. Nishat, and S. Ahmed, "Numerical simulation studies of $Cs_3Bi_2I_9$ perovskite solar device with optimal selection of electron and hole transport layers," Optik **231**, 166417 (2021).

[43]F. Bai, Y. Hu, Y. Hu, T. Qiu, X. Miao, and S. Zhang, "Lead-free, air-stable ultrathin $Cs_3Bi_2I_9$ perovskite nanosheets for solar cells," Sol. Energy Mater. Sol. Cells **184**, 15–21 (2018).

[44]B.-M. Bresolin, C. Günnemann, D. W. Bahnemann, and M. Sillanpää, "Pb-Free $Cs_3Bi2I_9$ perovskite as a visible-light-active photocatalyst for organic pollutant degradation," Nanomaterials **10**(4), 763 (2020).

[45]Z. Qi, X. Fu, T. Yang, D. Li, P. Fan, H. Li, F. Jiang, L. Li, Z. Luo, X. Zhuang, and A. Pan, "Highly stable lead-free $Cs_3Bi_2I_9$ perovskite nanoplates for photodetection applications," Nano Res. **12**(8), 1894–1899 (2019).

[46]L. Peedikakkandy, S. Chatterjee, and A. J. Pal, "Bandgap engineering and efficient conversion of a ternary perovskite $(Cs_3Bi_2I_9)$ to a double perovskite $(Cs_2NaBiI_6)$ with the aid of alkali metal sulfide," J. Phys. Chem. C **124**(20), 10878–10886 (2020).

[47]Y. Li, Z. Shi, W. Liang, J. Ma, X. Chen, D. Wu, Y. Tian, X. Li, C. Shan, and X. Fang, "Recent advances toward environment-friendly photodetectors based

on lead-free metal halide perovskites and perovskite derivatives," Mater. Horiz. **8**(5), 1367–1389 (2021).

[48]A. K. Geim and I. V. Grigorieva, "Van der Waals heterostructures," Nature **499**(7459), 419–425 (2013).

[49]A. Bafekry and M. Neek-Amal, "Tuning the electronic properties of graphene-graphitic carbon nitride heterostructures and heterojunctions by using an electric field," Phys. Rev. B **101**(8), 085417 (2020).

[50]M. D. Tran, H. Kim, J. S. Kim, M. H. Doan, T. K. Chau, Q. A. Vu, J.-H. Kim, and Y. H. Lee, "Two-terminal multibit optical memory via van der Waals heterostructure," Adv. Mater. **31**(7), 1807075 (2019).

[51]M. Yao, T. Wu, B. Liu, J. Li, and M. Long, "First principle study on interfacial interaction of black phosphorus and CsBr VdW heterostructure," Phys. Lett. A **384**(25), 126614 (2020).

[52]Q.-H. Li, Y.-F. Ding, P.-B. He, R. Zeng, Q. Wan, and M.-Q. Cai, "Transition of the type of band alignments for all-inorganic perovskite van der Waals heterostructures $CsSnBr_3/WS_{2(1−x)}Se_{2x}$," J. Phys. Chem. Lett. **12**(15), 3809–3818 (2021).

[53]C.-S. Liao, Q.-Q. Zhao, Y.-Q. Zhao, Z.-L. Yu, H. Zhou, P.-B. He, J.-L. Yang, and M.-Q. Cai, "First-Principles investigations of electronic and optical properties in the $MoS_2/CsPbBr_3$ heterostructure," J. Phys. Chem. Solids **135**, 109060 (2019).

[54]Y.-Q. Zhao, Y. Xu, D.-F. Zou, J.-N. Wang, G.-F. Xie, B. Liu, M.-Q. Cai, and S.-L. Jiang, "First-principles study on photovoltaic properties of 2D $Cs_2PbI_4$-black phosphorus heterojunctions," J. Phys. Condens. Matter **32**(19), 195501 (2020).

[55]J. He, J. Su, Z. Lin, S. Zhang, Y. Qin, J. Zhang, J. Chang, and Y. Hao, "Theoretical studies of electronic and optical behaviors of all-inorganic $CsPbI_3$and two-dimensional $MS_2$(M = Mo, W) heterostructures," J. Phys. Chem. C **123**(12), 7158–7165 (2019).

[56]Y.-L. Hong, Z. Liu, L. Wang, T. Zhou, W. Ma, C. Xu, S. Feng, L. Chen, M.-L. Chen, D.-M. Sun, X.-Q. Chen, H.-M. Cheng, and W. Ren, "Chemical vapor deposition of layered two-dimensional $MoSi_2N_4$ materials," Science **369**(6504), 670–674 (2020).

[57]A. Bafekry, M. Faraji, D. M. Hoat, M. M. Fadlallah, M. Shahrokhi, F. Shojaei, D. Gogova, and M. Ghergherehchi, "$MoSi_2N_4$ single-layer: A novel two-dimensional material with outstanding mechanical, thermal, electronic, optical, and photocatalytic properties," arXiv:2009.04267 Cond-Mat Physicsphysics (2020).

[58]G. Kresse and D. Joubert, "From ultrasoft pseudopotentials to the projector augmented-wave method," Phys. Rev. B **59**(3), 1758–1775 (1999).

[59]G. Kresse and J. Furthmüller, "Efficient iterative schemes for ab initio total-energy calculations using a plane-wave basis set," Phys. Rev. B **54**(16), 11169–11186 (1996).

[60]P. E. Blöchl, "Projector augmented-wave method," Phys. Rev. B **50**(24), 17953–17979 (1994).

[61]J. P. Perdew, K. Burke, and M. Ernzerhof, "Generalized gradient approximation made simple," Phys. Rev. Lett. **77**(18), 3865–3868 (1996).

[62]B. Chabot and E. Parthi, "$Cs_3Sb_2I_9$ and $Cs_3B_2I_9$ with the hexagonal $Cs_3Cr_2Cl_9$ structure Type. 4," Acta Crystallographica Section B: Structural Crystallography and Crystal Chem. **34**(2): 645–648 (1978).

[63]M. Farmanbar and G. Brocks, "First-principles study of van der Waals interactions and lattice mismatch at $MoS_2$/metal interfaces," Phys. Rev. B **93**(8), 085304 (2016).

[64]H. Zhong, W. Xiong, P. Lv, J. Yu, and S. Yuan, "Strain-induced semiconductor to metal transition in $MA_2Z_4$ bilayers (M = Ti, Cr, Mo ; A = Si ; Z = N, P)," Phys. Rev. B **103**(8), 085124 (2021).

[65]B. Gao, J.-R. Zhang, L. Chen, J. Guo, S. Shen, C.-T. Au, S.-F. Yin, and M.-Q. Cai, "Density functional theory calculation on two-dimensional $MoS_2$/ BiOX (X = Cl, Br, I) van der Waals heterostructures for photocatalytic action," Appl. Surf. Sci. **492**, 157–165 (2019).

[66]B. Zheng, C. Ma, D. Li, J. Lan, Z. Zhang, X. Sun, W. Zheng, T. Yang, C. Zhu, G. Ouyang, G. Xu, X. Zhu, X. Wang, and A. Pan, "Band alignment engineering in two-dimensional lateral heterostructures," J. Am. Chem. Soc. **140**(36), 11193–11197 (2018).

[67]S. Tongay, W. Fan, J. Kang, J. Park, U. Koldemir, J. Suh, D. S. Narang, K. Liu, J. Ji, J. Li, R. Sinclair, and J. Wu, "Tuning interlayer coupling in large-area heterostructures with CVD-grown $MoS_2$ and $WS_2$ monolayers," Nano Lett. **14**(6), 3185–3190 (2014).

[68]X. Hong, J. Kim, S.-F. Shi, Y. Zhang, C. Jin, Y. Sun, S. Tongay, J. Wu, Y. Zhang, and F. Wang, "Ultrafast charge transfer in atomically thin $MoS_2/WS_2$ heterostructures," Nat. Nanotechnol. **9**(9), 682–686 (2014).

[69]C.-H. Lee, G.-H. Lee, A. M. van der Zande, W. Chen, Y. Li, M. Han, X. Cui, G. Arefe, C. Nuckolls, T. F. Heinz, J. Guo, J. Hone, and P. Kim, "Atomically thin p-n junctions with van der Waals heterointerfaces," Nat. Nanotechnol. **9**(9), 676–681 (2014).

[70]J. Kang, S. Tongay, J. Zhou, J. Li, and J. Wu, "Band offsets and heterostructures of two-dimensional semiconductors," Appl. Phys. Lett. **102**(1), 012111 (2013).

[71]L. Fu, Y. Wan, N. Tang, Y. Ding, J. Gao, J. Yu, H. Guan, K. Zhang, W. Wang, C. Zhang, J. Shi, X. Wu, S.-F. Shi, W. Ge, L. Dai, and B. Shen, "K-l crossover transition in the conduction band of monolayer $MoS_2$ under hydrostatic pressure," Sci. Adv. **3**(11), e1700162 (2017).

[72]K. D. Pham, N. N. Hieu, H. V. Phuc, I. A. Fedorov, C. A. Duque, B. Amin, and C. V. Nguyen, "Layered graphene/GaS van der Waals heterostructure: Controlling the electronic properties and Schottky barrier by vertical strain," Appl. Phys. Lett. **113**(17), 171605 (2018).

[73]L. Zhang, Y. Tang, A. R. Khan, M. M. Hasan, P. Wang, H. Yan, T. Yildirim, J. F. Torres, G. P. Neupane, Y. Zhang, Q. Li, and Y. Lu, "2D materials and heterostructures at extreme pressure," Adv. Sci. **7**(24), 2002697 (2020).

[74]L. Zhang, C. Liu, L. Wang, C. Liu, K. Wang, and B. Zou, "Pressure-induced emission enhancement, band-gap narrowing, and metallization of halide perovskite $Cs_3Bi_2I_9$," Angew. Chem. Int. Ed. **57**(35), 11213–11217 (2018).

[75]X.-H. Li, B.-J. Wang, X.-L. Cai, L.-W. Zhang, G.-D. Wang, and S.-H. Ke, "Tunable electronic properties of arsenene/GaS van der Waals heterostructures," RSC Adv. **7**(45), 28393–28398 (2017).

[76]H. Zhong, K. Huang, G. Yu, and S. Yuan, "Electronic and mechanical properties of few-layer borophene," Phys. Rev. B **98**(5), 054104 (2018).

[77]C. Chen, H. Lv, P. Zhang, Z. Zhuo, Y. Wang, C. Ma, W. Li, X. Wang, B. Feng, P. Cheng, X. Wu, K. Wu, and L. Chen, "Synthesis of bilayer borophene," Nat. Chem. **14**(1), 25–31 (2022).

[78]X. Liu, Q. Li, Q. Ruan, M. S. Rahn, B. I. Yakobson, and M. C. Hersam, "Borophene synthesis beyond the single-atomic-layer limit," Nat. Mater. **21**(1), 35–40 (2022).